

# *In situ* Identification of Reaction Intermediates and Mechanistic Understandings of Methane Oxidation over Hematite: A Combined Experimental and Theoretical Study

Yulian He<sup>1,2</sup>, Facheng Guo<sup>2,3</sup>, Ke R. Yang<sup>2,3</sup>, Jake A. Heinlein<sup>1,2</sup>, Scott M. Bamonte<sup>4</sup>, Jared J. Fee<sup>4</sup>, Shu Hu<sup>1,2</sup>, Steven L. Suib<sup>4</sup>, Gary L. Haller<sup>1</sup>, Victor S. Batista<sup>2,3</sup>, Lisa D. Pfefferle<sup>1</sup>

<b>Characterization Details</b> .....	S3
<b>Flow Reactor Setup</b> .....	S4
<b>Complete Mass Spectra</b> .....	S5
<b>Reaction Stoichiometry</b> .....	S6
<b>Blank control test</b> .....	S7
<b>Light-off curve upon a large mass loading</b> .....	S8
<b>Comparison of typical catalytic systems in CMC</b> .....	S9
<b>Bulk hematite with a large mass loading</b> .....	S10
<b>Post-reaction TEM/SEM analyses</b> .....	S11
<b>X-ray Photoelectron Spectroscopy analyses</b> .....	S12
<b>Arrhenius plot</b> .....	S13
<b>Reaction models</b> .....	S14
<b>Temperature-programmed isotopic oxygen-exchange</b> .....	S15
<b>Self-dehydration in the TPR</b> .....	S16
<b>Hematite nanosheets react with pure CH<sub>4</sub></b> .....	S17
<b><i>In situ</i> DRIFTS spectra of water desorption and CO<sub>2</sub></b> .....	S18
<b>Models of different hematite facets</b> .....	S19

<b>Self-dehydrated model surface .....</b>	<b>S20</b>
<b>Hydrogen atom parking slabs .....</b>	<b>S21</b>
<b>CH<sub>4</sub> adsorption on different sites .....</b>	<b>S22</b>
<b>Proposed electron transfer processes.....</b>	<b>S23</b>
<b>Calculated energy barrier of the PCET process .....</b>	<b>S24</b>
<b>Magnetic Moment Parameters .....</b>	<b>S25</b>
<b>Reference .....</b>	<b>S26</b>

## Characterization Details

**Scanning Electron Microscopy (SEM) and Transmission Electron Microscopy (TEM).** SEM and TEM images were collected on a Hitachi SU-70 and FEI Tecnai Osiris, respectively. The acceleration voltage was 15 kV for SEM and 200 kV for TEM. For SEM, powder samples were pressed onto a double-sided carbon tape, while TEM samples were dispersed in ethanol via sonication and then added dropwise to a holey carbon-coated copper grid. In all cases multiple spots were examined to ensure sample uniformity.

**X-ray Photoelectron Spectroscopy (XPS).** The XPS spectra were collected using a monochromatic 1486.7 eV Al K $\alpha$  X-ray source on PHI VersaProbe II X-ray Photoelectron Spectrometer with a 0.47 eV system resolution. The energy scale has been calibrated using Cu 2p $_{3/2}$  (932.67 eV) and Au 4f $_{7/2}$  (84.00 eV) peaks on a clean copper plate and a clean gold foil, respectively. Powder samples were pressed onto a double-sided scotch tape on a substrate. For region scan, high power (100u100W20kV\_HP), 23.500 eV Pass Energy and 0.1000 eV step size were used, and each spectrum was swept 10 times to improve the signal/noise ratio. Data analysis was performed with a software package in MultiPak and CasaXPS. Atomic concentrations were calculated as suggested by the following equation:

$$AC_1(\%) = \frac{A_1/R.S.F}{A_1/R.S.F + \dots + A_n/R.S.F} \quad (S1)$$

where  $AC_1$  is the atomic concentration for element 1,  $A_n$  is the integrated peak area for element n and R.S.F is the relative structural factor.

**Brunauer-Emmett-Teller (BET)-N $_2$  Physisorption.** Surface area measurements were performed using a Micromeritics ASAP 2460. Adsorption-Desorption isotherms were constructed using an 11-point Brunauer, Emmett and Teller (BET) measurements protocol with N $_2$  as the adsorbate. Typically, around 100 mg of sample was used and outgassed at 200°C overnight before measurements.

## Flow Reactor Setup

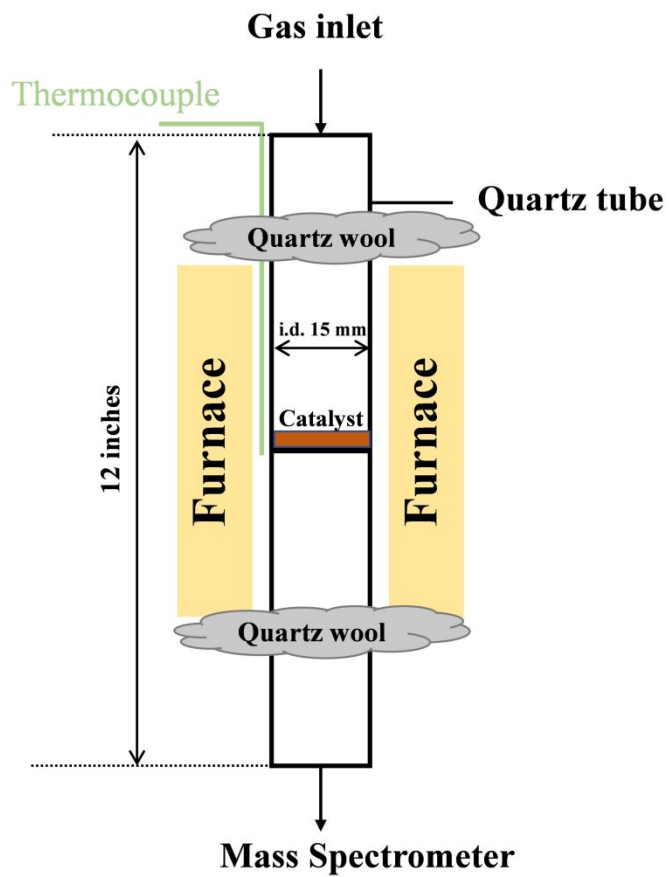


**Fig. S1** Schematic illustration of the flow reactor setup.

## Complete Mass Spectra

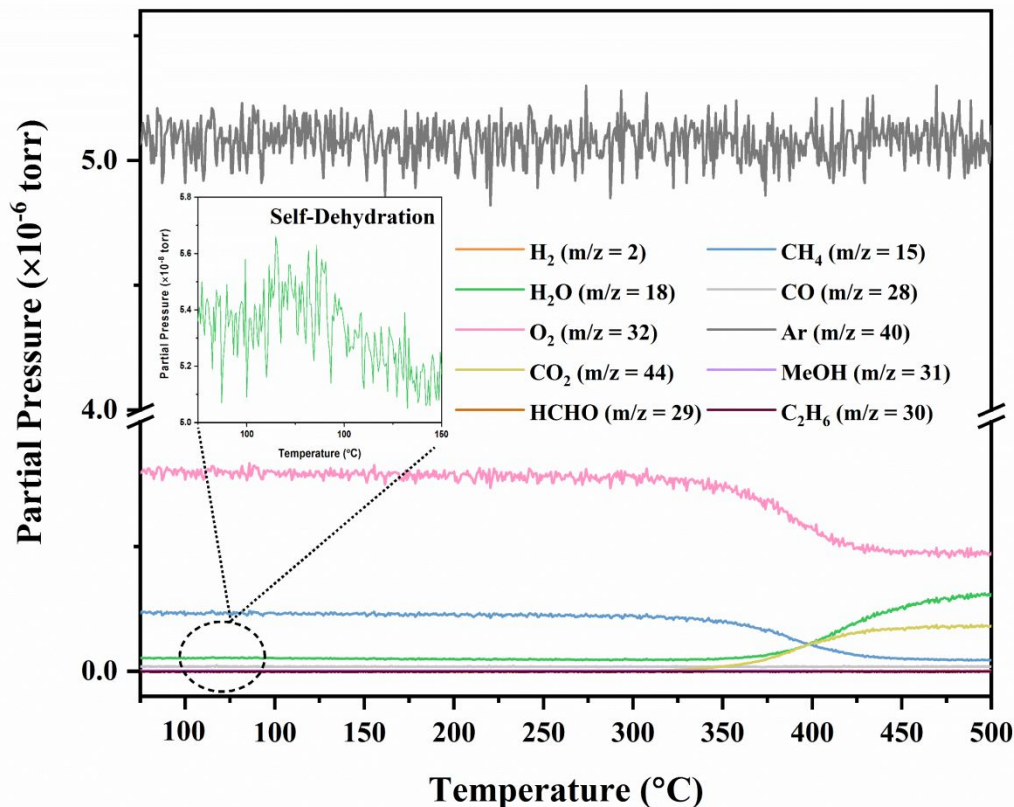


**Fig. S2** Complete mass spectra of the methane catalytic combustion experiment on hematite nanosheets with selected representative channels. The  $\text{CH}_4$  was combusted into  $\text{CO}_2$  and  $\text{H}_2\text{O}$  with 100% selectivity, no other by-products were detected. Dehydration was observed near  $100^\circ\text{C}$ , which is likely due to the -OH termination from the hematite nanosheet structure itself. No change in Argon signal was observed indicating that the pressure in the chamber remained constant.

## Reaction Stoichiometry

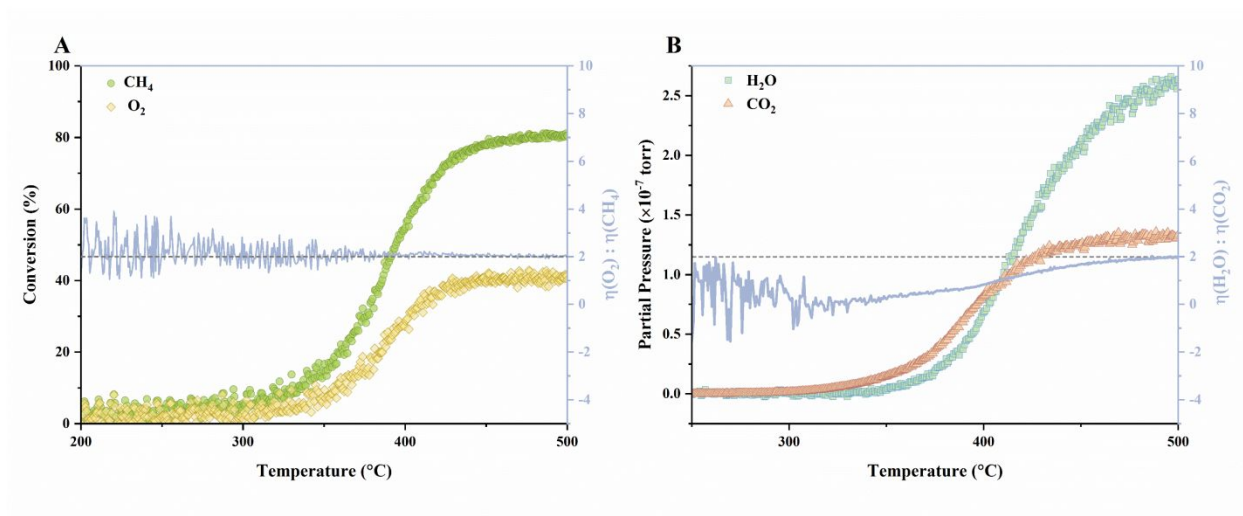


**Fig. S3** Reaction stoichiometry of the methane catalytic combustion on hematite nanosheets: **A)** Reactants; **B)** Products. Both the stoichiometric ratios of (A) O<sub>2</sub> to CH<sub>4</sub> consumption and (B) H<sub>2</sub>O to CO<sub>2</sub> production are close to 2 at high temperatures, consistent with a typical methane complete oxidation reaction. The stoichiometric ratio is below 2 initially for H<sub>2</sub>O to CO<sub>2</sub> production at lower temperatures as the water forms and leaves the surface later than CO<sub>2</sub> does.

## Blank control test

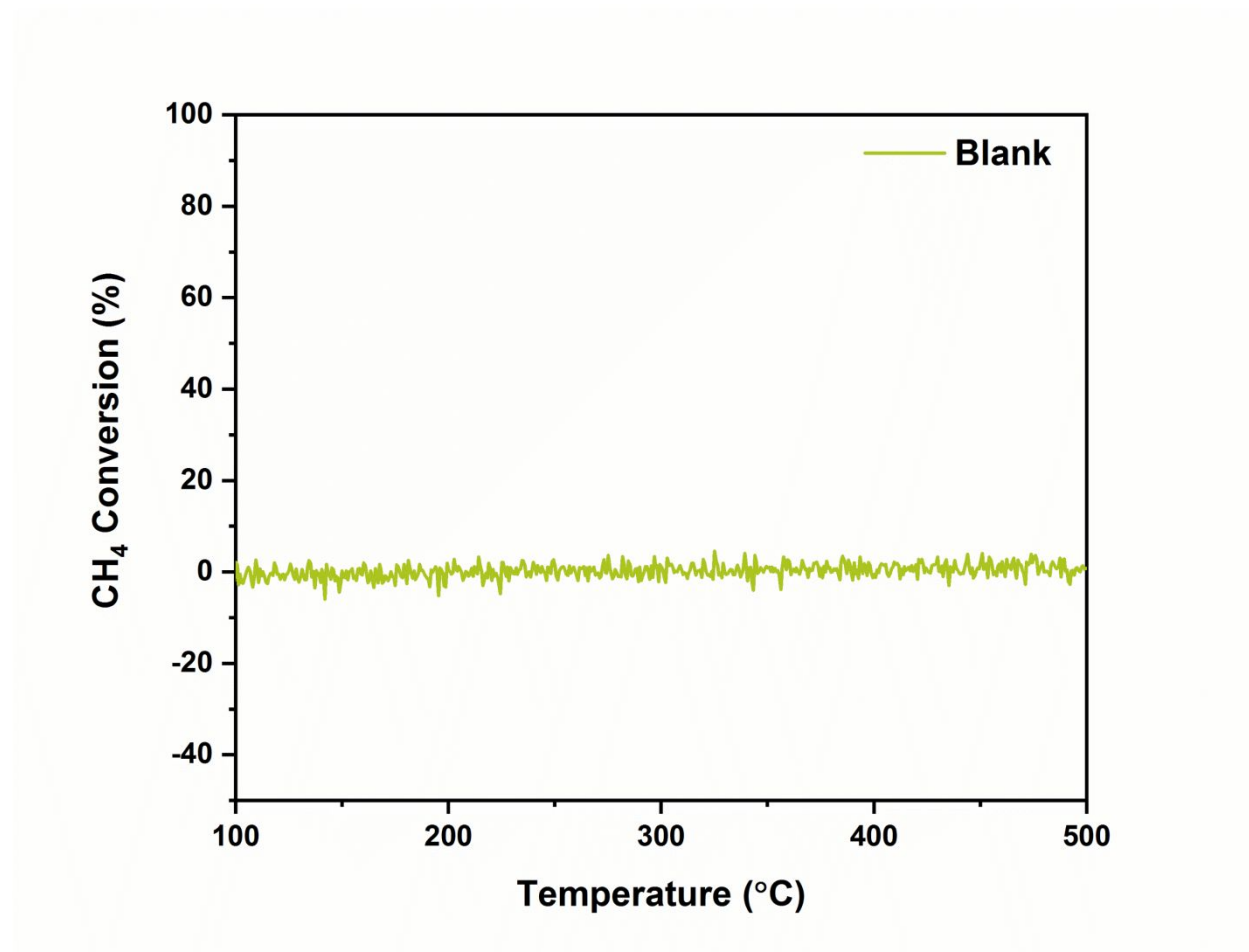


**Fig. S4** The blank test with the same composited gas feeds (5% CH<sub>4</sub> (WHSV = 10000 mL·g<sup>-1</sup>·h<sup>-1</sup>), 20% O<sub>2</sub>, and 75% Ar) and the same procedures in the absence of any catalysts shows no conversion of CH<sub>4</sub>.

## Light-off curve upon a large mass loading

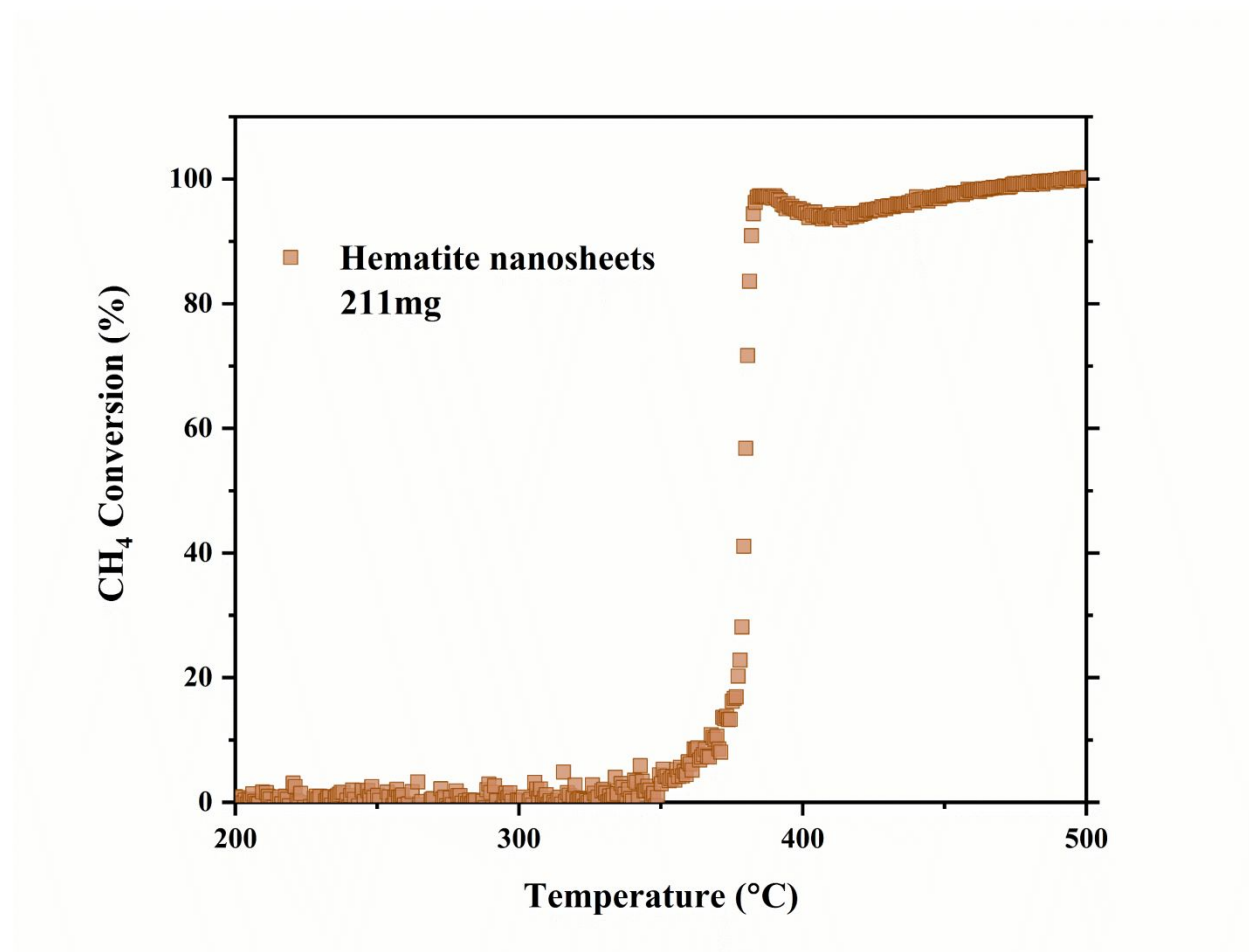


**Fig. S5** The catalytic light-off curve of hematite nanosheets in CMC reaction with a 211 mg of mass loading, showing 100% methane conversion. The reason for the slight decrease in activity after the first peak at 100% is similar to that occurred during the thermal stability test as discussed in Fig. 1d. This is due to the increased local temperature caused by the heat release from the combustion reaction itself, after the steady state is reached, the activity stabilizes at 100%.



# Comparison of typical catalytic systems in CMC

**Table S1. Comparisons of important reaction parameters with several typical catalysts**

Catalyst	Mass/ mg	Surface Area/ m <sup>2</sup> ·g <sup>-1</sup>	Gas feed-in conditions	CH <sub>4</sub> Space Velocity /mL·g <sub>cat</sub> <sup>-1</sup> ·h <sup>-1</sup>	T <sub>50</sub> / °C	<sup>a</sup> Specific reaction rate at T <sub>50</sub> /10 <sup>-3</sup> mmol·g <sub>cat</sub> <sup>-1</sup> ·s <sup>-1</sup>	E <sub>a</sub> /kJ·mol <sup>-1</sup>	Ref
<b>Noble metal</b>								
Pd@CeO <sub>2</sub> /Al <sub>2</sub> O <sub>3</sub>	25	100	0.5%CH <sub>4</sub> , 2%O <sub>2</sub> in Ar	1,000	320	6.20	103	[1]
Pd/H-ZMS-5	200	-	1%CH <sub>4</sub> , 20%O <sub>2</sub> in N <sub>2</sub>	150	300	0.93	84.7	[2]
Pd/SiO <sub>2</sub>	50	688	0.3%CH <sub>4</sub> , 2.4%O <sub>2</sub> in He	180	355	1.12	84	[3]
<b>Bimetallic</b>								
Pd <sub>50</sub> Pt <sub>50</sub> /Al <sub>2</sub> O <sub>3</sub>	100	107	1.5% CH <sub>4</sub> in air	3,750	880	23.25	-	[4]
3%AuPd/3DOM- La <sub>0.6</sub> Sr <sub>0.4</sub> MnO <sub>3</sub>	20	33.8	5%CH <sub>4</sub> , 30%O <sub>2</sub> in N <sub>2</sub>	2,500	314	15.50	46.3	[5]
<b>Single metal oxide</b>								
6%CuO/ZrO <sub>2</sub>	200	36	1.4%CH <sub>4</sub> , 6%O <sub>2</sub> in He	420	500	2.60	96	[6]
<b>2D α-Fe<sub>2</sub>O<sub>3</sub></b>	<b>30</b>	<b>166</b>	<b>5%CH<sub>4</sub>, 20%O<sub>2</sub> in Ar</b>	<b>10,000</b>	<b>394</b>	<b>62.00</b>	<b>73.64</b>	<b>This work</b>
<b>Bulk α-Fe<sub>2</sub>O<sub>3</sub></b>	<b>900</b>	<b>5.38</b>	<b>5%CH<sub>4</sub>, 20%O<sub>2</sub> in Ar</b>	<b>333</b>	<b>384</b>	<b>2.07</b>	<b>-</b>	<b>This work</b>
α-MnO <sub>2</sub>	20	69.8	2%CH <sub>4</sub> , 20%O <sub>2</sub> in Ar	420	463	2.60	-	[7]
<b>Perovskite</b>								
LaSrCuO <sub>4</sub>	100	11.9	2%CH <sub>4</sub> , 20%O <sub>2</sub> in N <sub>2</sub>	1,000	620	6.20	-	[8]
3DOM- La <sub>0.6</sub> Sr <sub>0.4</sub> MnO <sub>3</sub>	20	32.4	5%CH <sub>4</sub> , 30%O <sub>2</sub> in N <sub>2</sub>	2,500	384	15.50	92.8	[5]
LaMnO <sub>3</sub>	20	8.2	2%CH <sub>4</sub> , 20%O <sub>2</sub> in Ar	420	619	2.60	-	[7]
<b>Spinel oxide</b>								
NiCo <sub>2</sub> O <sub>4</sub>	500	218.7	5%CH <sub>4</sub> , 25%O <sub>2</sub> in Ar	1,200	260	7.44	108	[9]
Co <sub>3</sub> O <sub>4</sub> @C	100	23.3	6.7%CH <sub>4</sub> , 16.75%O <sub>2</sub> in He	1,206	376	7.48	68	[10]
CoAlO	20	88.6	2%CH <sub>4</sub> , 20%O <sub>2</sub> in N <sub>2</sub>	600	538	3.72	96.7	[11]

a. Due to the ambiguity of determining the real number of active sites in metal oxide systems, the specific reaction rate is instead calculated to compare with other systems rather than the turnover frequency. However, in this way, the specific rate for non-supported systems will be more augmented than that of the supported systems. For these comparisons, other parameters such as the apparent activation energy will be considered in conjunction.

## Bulk hematite with a large mass loading

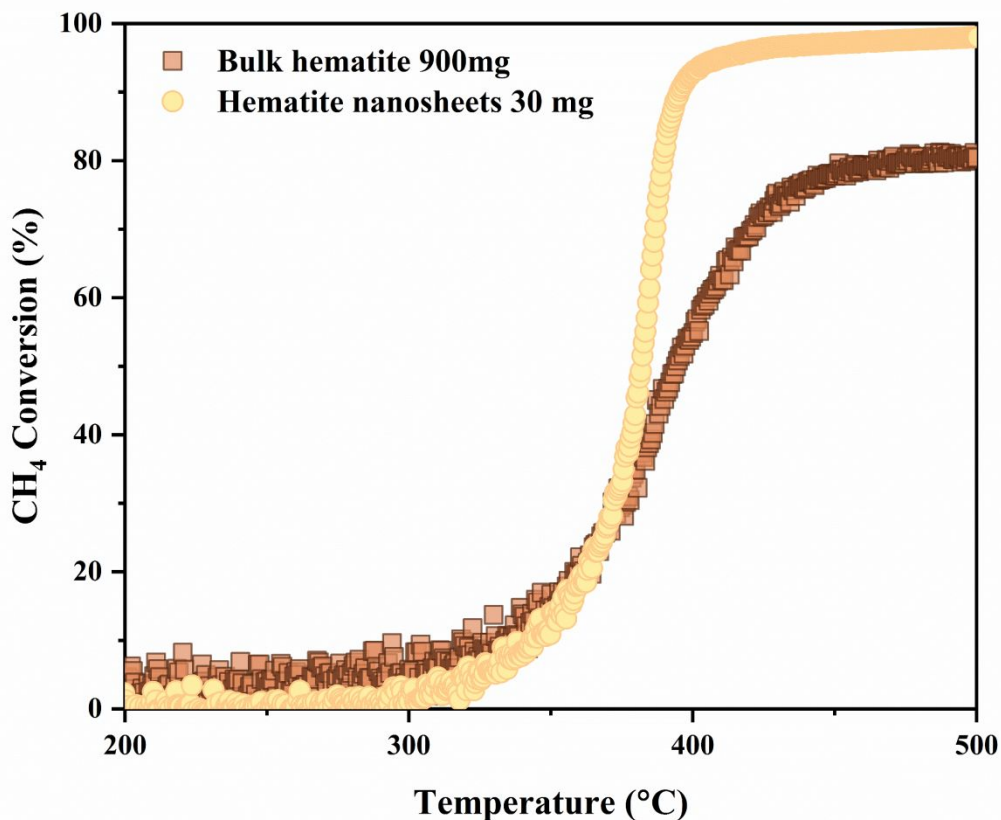


**Fig. S6** The light-off curve of bulk hematite with a mass loading of 900 mg in methane combustion experiment with 100% conversion and a  $T_{50}$  of 382°C compared to the light-off curve of hematite nanosheets with 30 mg mass loading. In this case, the total surface area of bulk catalyst is almost comparable to that of 30 mg of the 2D nanosheets. The performance is quite similar in both scenarios, suggesting that hematite is reactive in methane combustion regardless of nano or bulk, however, upon the same mass loading, 2D structure is more advantageous owing to the large surface area and high density of active sites exposed per unit mass.

## Post-reaction TEM/SEM analyses

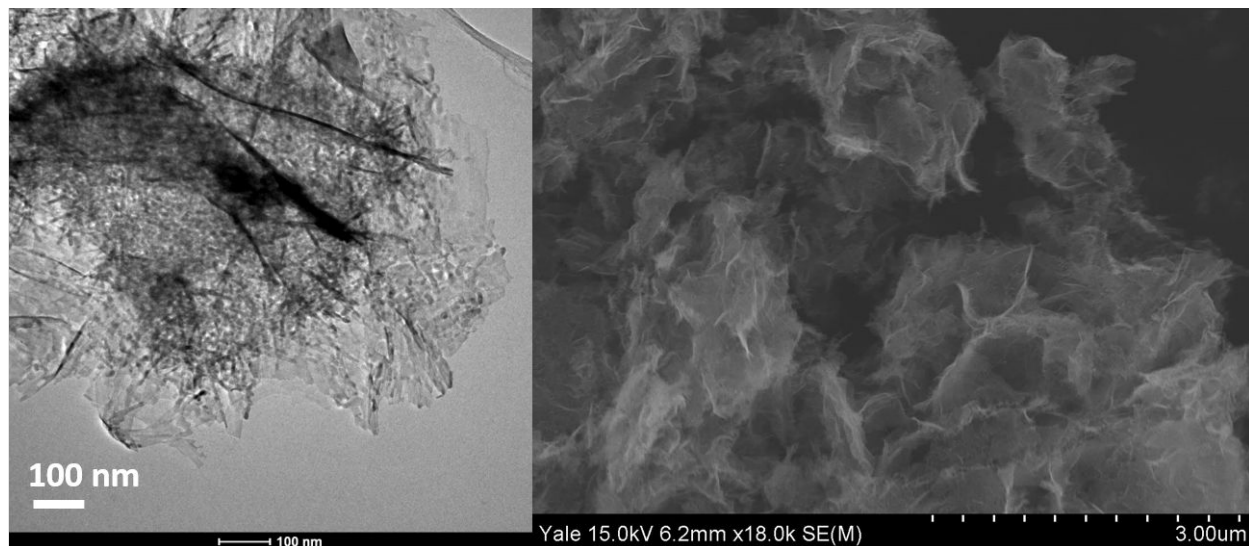


**Fig. S7** The morphology of nanosheet structure was largely maintained after the CMC reaction from both TEM on the left and SEM on the right. Multiple spots were examined to ensure uniformity.

## X-ray Photoelectron Spectroscopy analyses

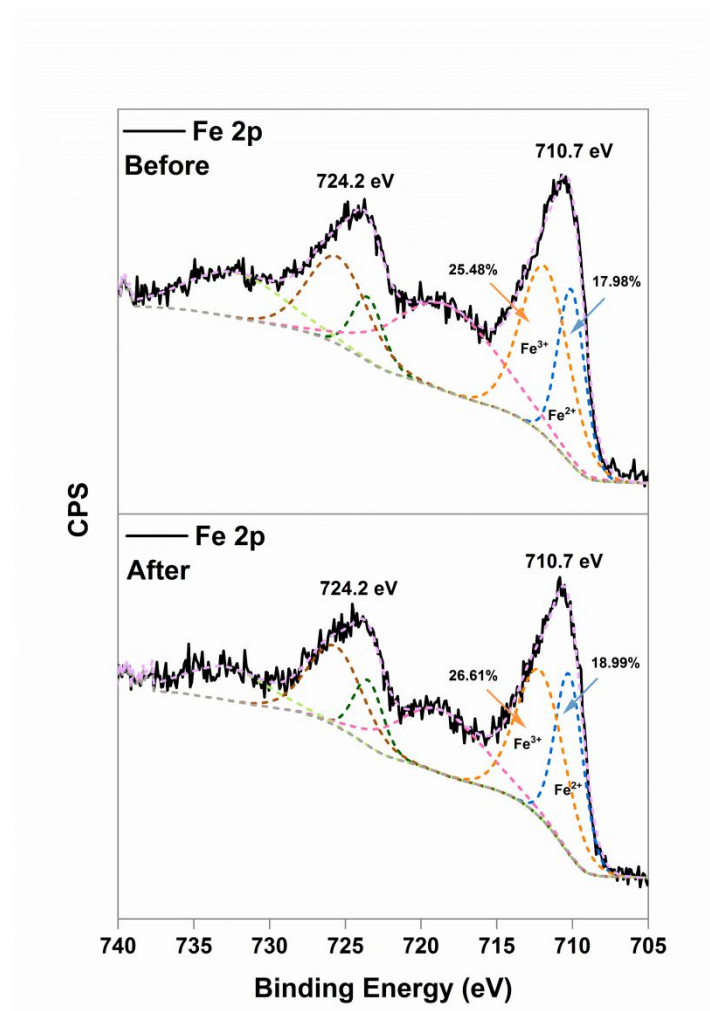


**Fig. S8** XPS analyses at Fe 2p before and after the combustion experiment. The oxidation state of Fe(III) and the surface atomic ratio of Fe:O = 2:3 (calculated according to equation (S1)) remained consistent.

## Arrhenius plot

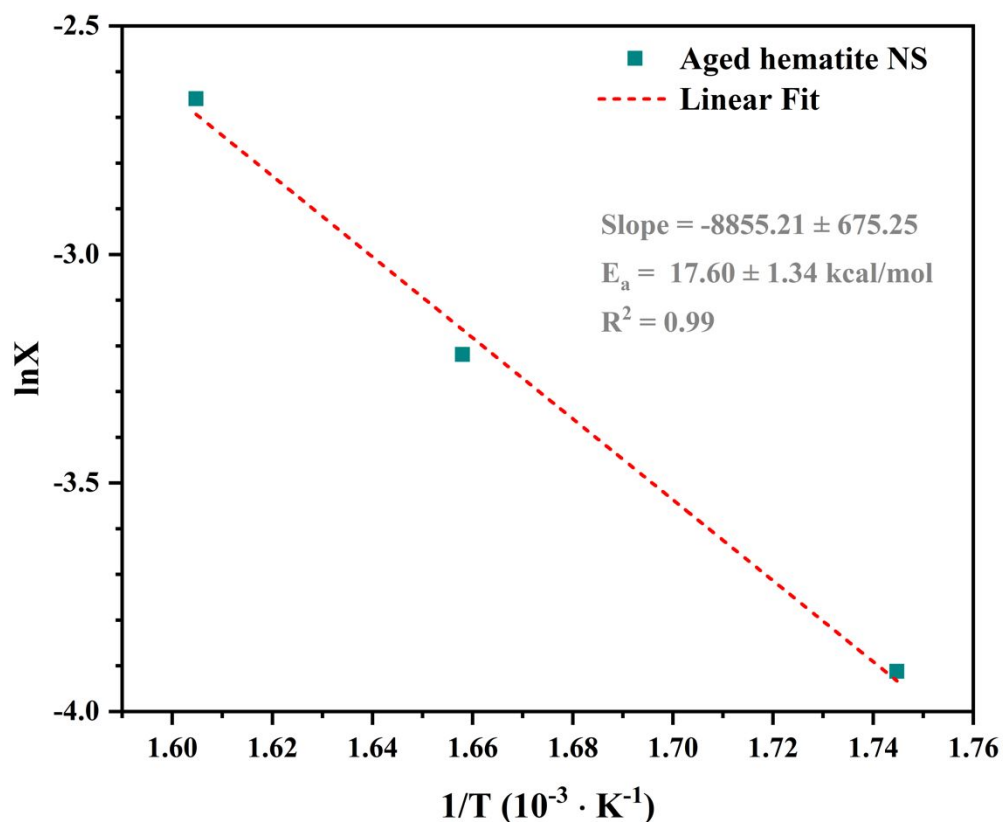


**Fig. S9** Arrhenius plot constructed through isothermal experiments at various temperatures. X is conversion. The same reactor setup was used for the measurements. For each run, 30 mg of the aged (used) hematite nanosheets were loaded and the reactor was brought up to the designated temperature rapidly from room temperature and dwelled for 2 hours until the steady state was reached. Each data point represents the  $CH_4$  conversion averaged during the steady state. The catalyst used in this experiment was cycled many times beforehand in order to get more reliable results.

## Reaction models

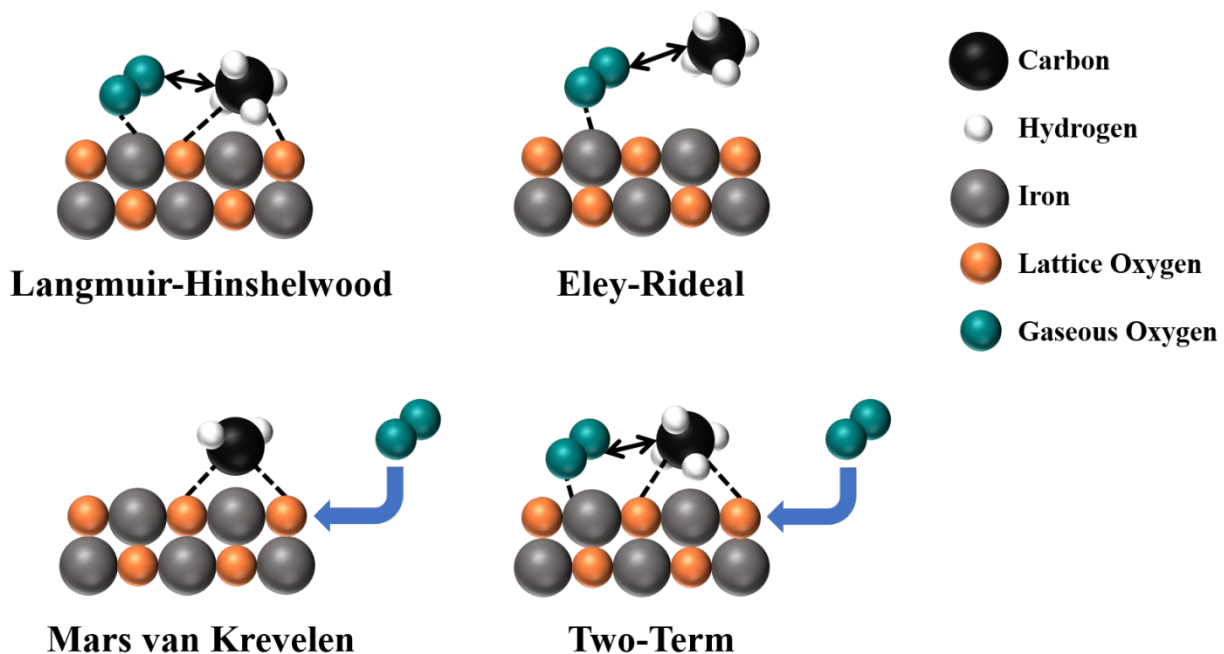


**Fig. S10** Schematic illustrations of the four reaction models. 1. *Langmuir-Hinshelwood* (LH) model: the surface reaction occurs through the dissociative/molecular adsorption of oxygen and adsorption of methane; 2. *Eley-Rideal* (ER) model: the surface reaction occurs through the dissociative adsorption of oxygen and gaseous methane; 3. *Mars van Krevelen* (MvK) redox model: through alternating reduction and oxidation of the catalyst surface; and 4. a two-term model (TT): the oxidation on the catalyst surface takes place by two routes: *via* the lattice oxygen and *via* the adsorbed oxygen

## Temperature-programmed isotopic oxygen-exchange

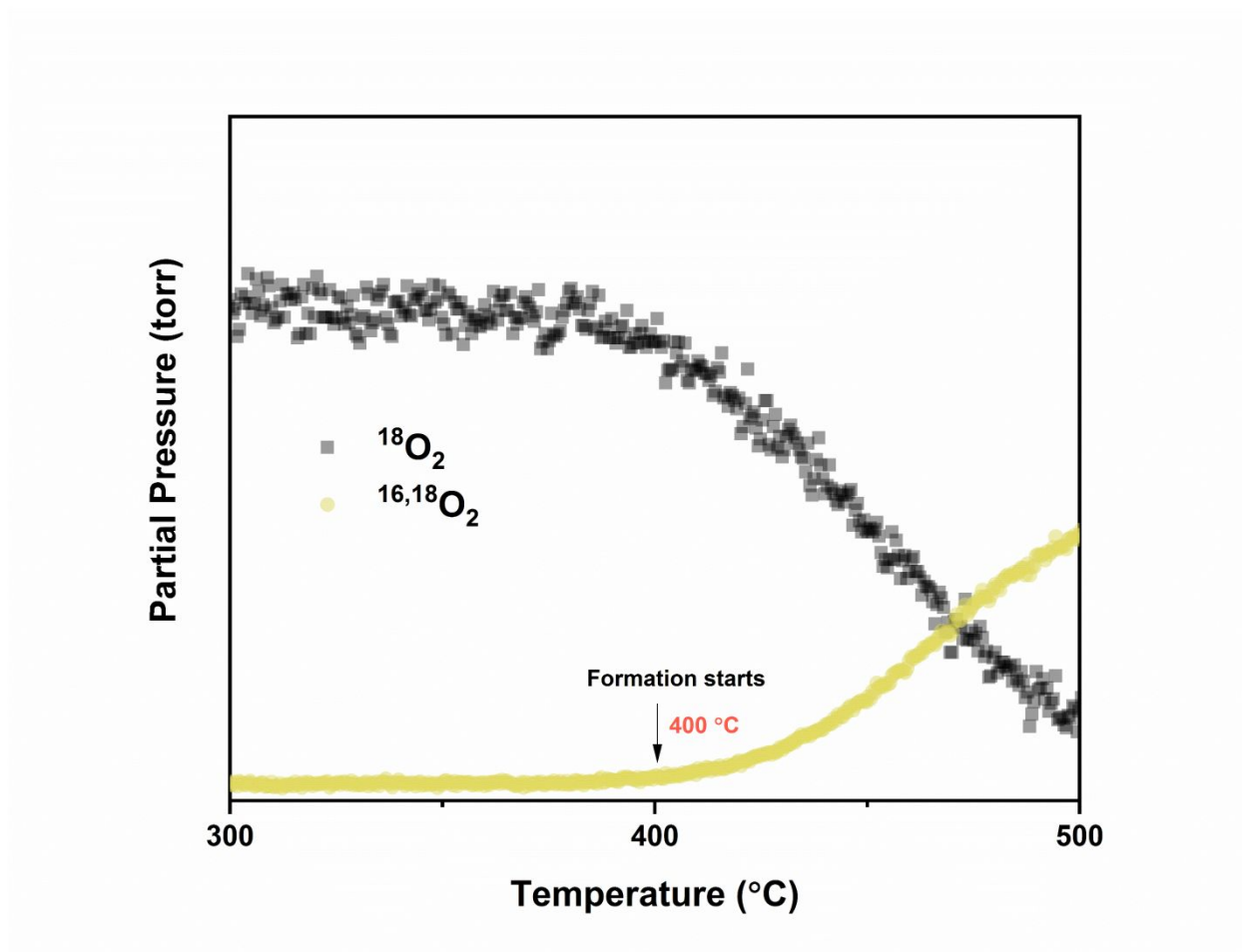


**Fig. S11** Temperature-programmed isotopic oxygen-exchange (TPIOE) experiment on hematite nanosheets. The result suggests that the lattice oxygen exchange with the gas phase oxygen did not start until around 400°C on pristine hematite nanosheets.

## Self-dehydration in the TPR

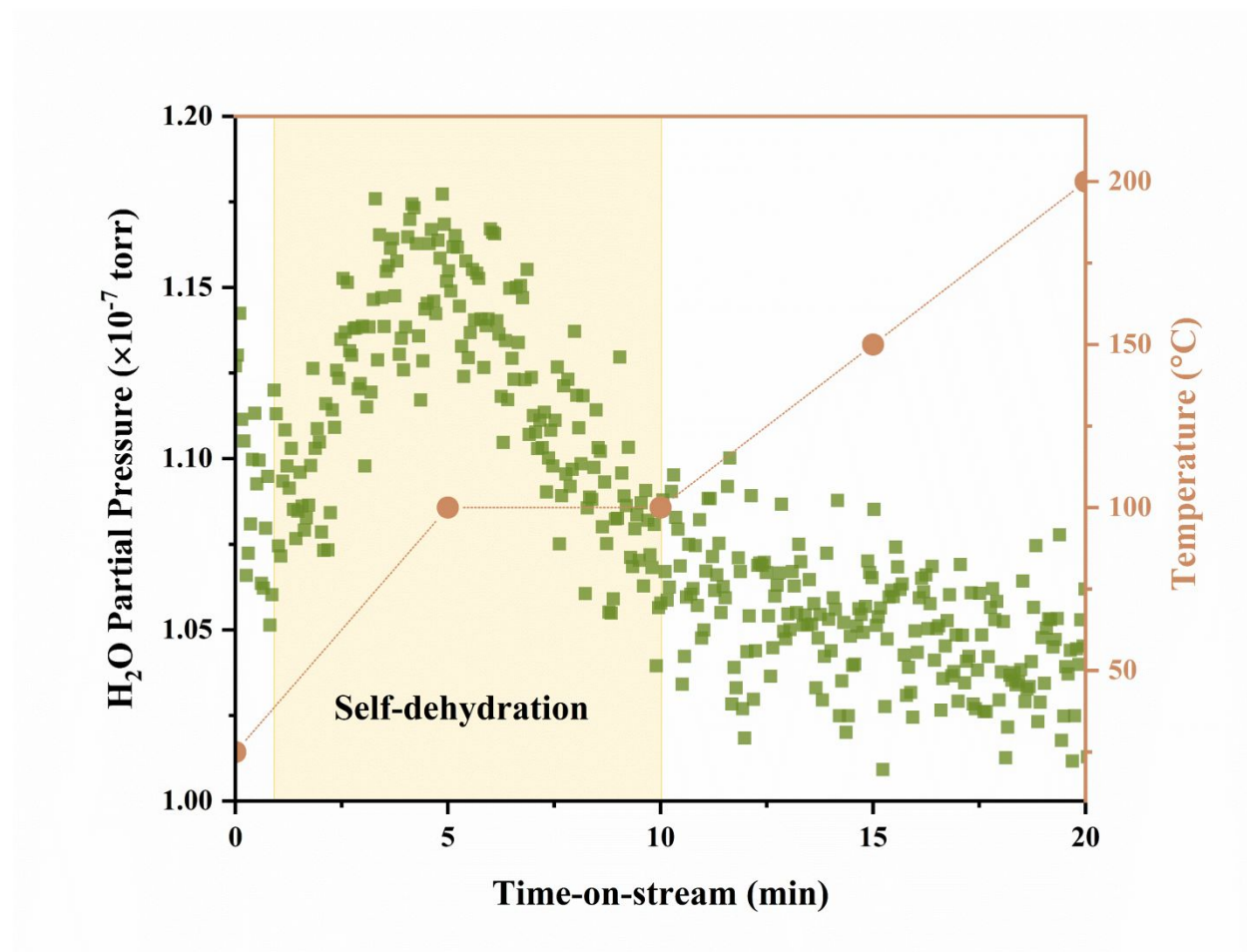


**Fig. S12** Water partial pressure channel in the CH<sub>4</sub>-TPR experiment. A similar self-dehydration behavior was observed as in the combustion experiment prior to the onset of the reaction at near 230°C.



## Hematite nanosheets react with pure CH<sub>4</sub>

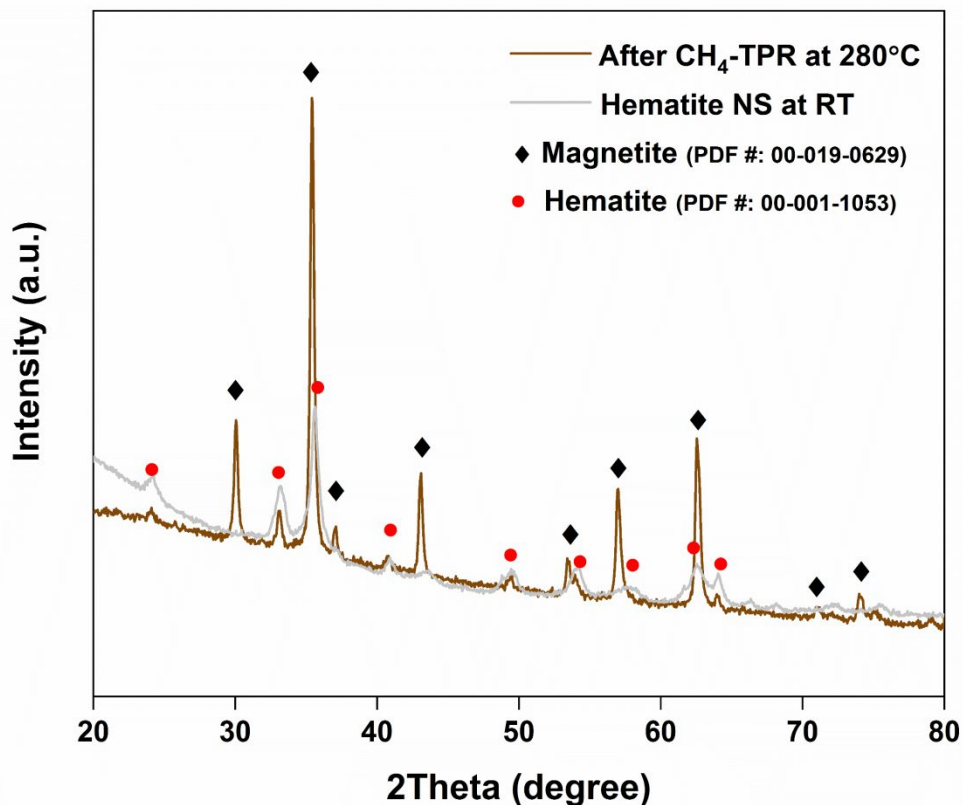


**Fig. S13** XRD patterns of hematite nanosheets after reacting with pure methane at 280°C. Part of hematite has been gradually reduced into magnetite without oxygen from the gas phase replenishing the vacancies. Noteworthy, compare to the XRD patterns of the pristine hematite nanosheets at room temperature, the peak broadening of the hematite component after the reduction remains highly unaltered, indicating a good thermal stability of the hematite nanosheets even under reductive environment.

## ***In situ* DRIFTS spectra of water desorption and CO<sub>2</sub>**

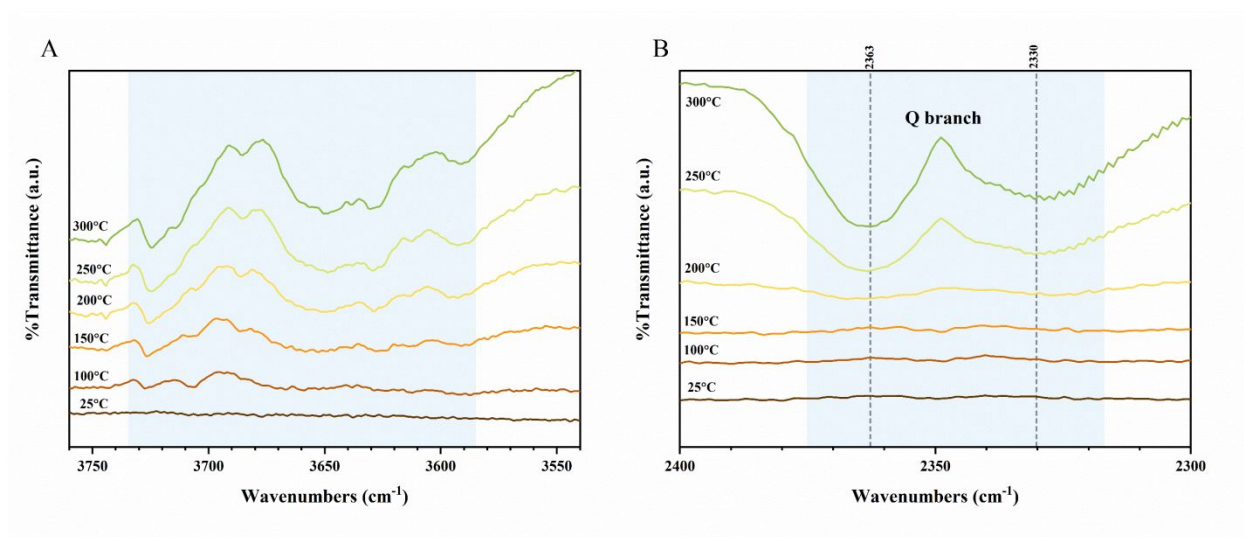
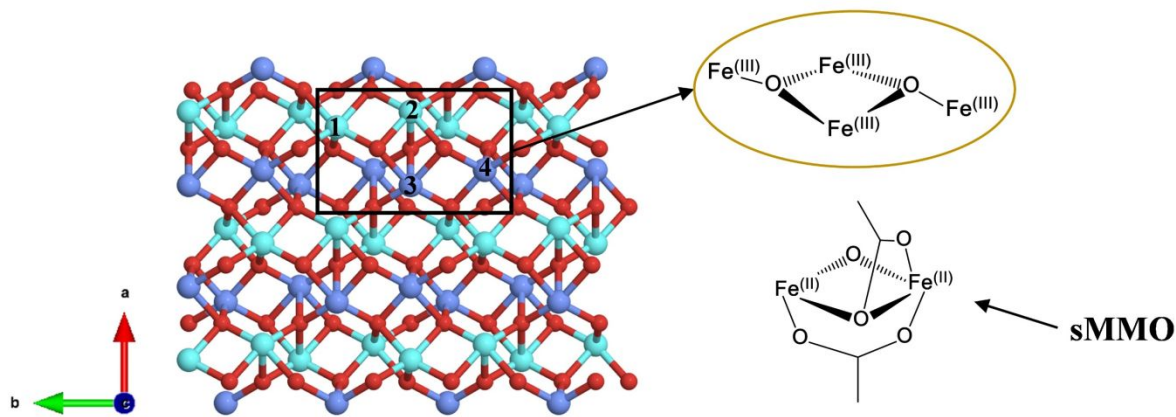


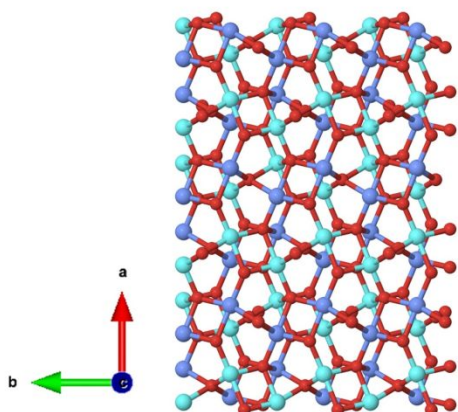
**Fig. S14** *In situ* DRIFTS spectra of **A)** broad water desorption peaks around 3590 – 3730 cm<sup>-1</sup>; **B)** CO<sub>2</sub> in the gas phase showing the characteristic P, Q, and R branches.

## Models of different hematite facets

### (a) (110) facet



### (b) (104) facet



### (c) (111) facet

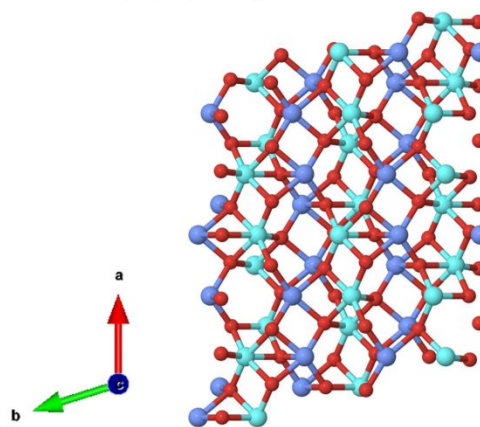


**Fig. S15** Supercells of different hematite facets with magnetic moments labeled. **a)** The (110) facet with the anti-ferromagnetic diiron couple on the surface, the proposed active center consists of such diiron couple with two additional adjacent irons as outlined in the black square; **b)** Supercell of (104) facet that does not contain the similar anti-ferromagnetic diiron center on the surface; **c)** Atomic magnetic moments along (111) plane. Color codes: red, dark blue, and light blue balls represent  $\text{O}^{2-}$ , spin-up  $\text{Fe}^{3+}$ , and spin-down  $\text{Fe}^{3+}$  ion, respectively. The oxidation state of Fe in the antiferromagnetic diiron couple in the active center of the soluble methane monooxygenase (sMMO) is proposed to be +2.<sup>12</sup>

## Self-dehydrated model surface

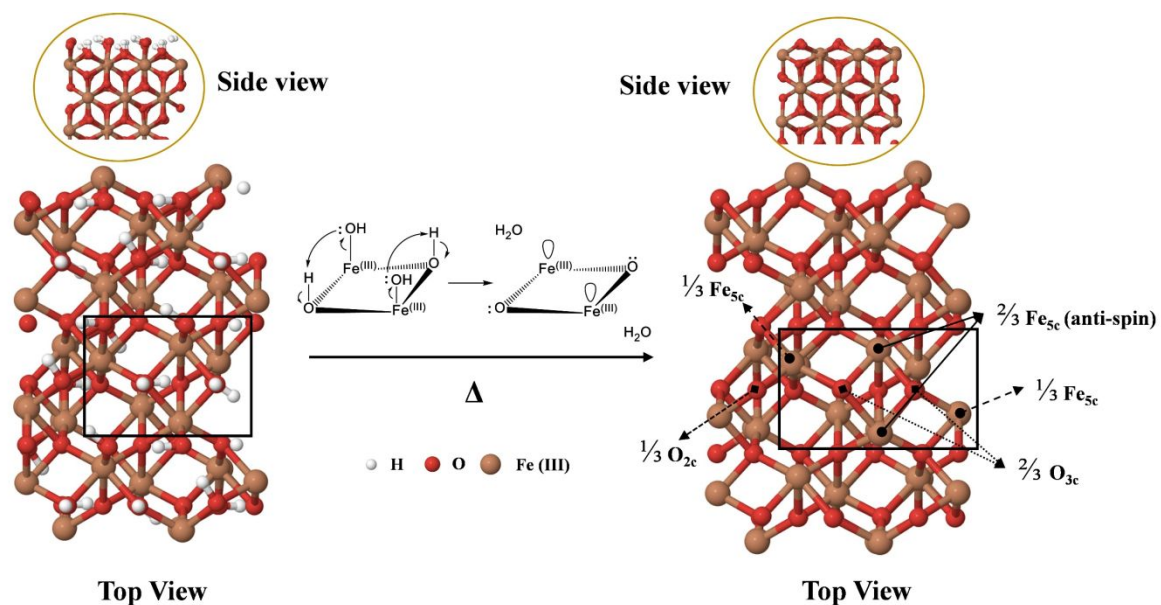


**Fig. S16** The proposed self-dehydration process on hematite (110) facet *via* an acid-base reaction at elevated temperatures prior to the onset of the combustion reaction. This will leave Fe(III) with 5 coordination and lone-paired electrons on the 3-coordinated oxygen.

## Hydrogen atom parking slabs

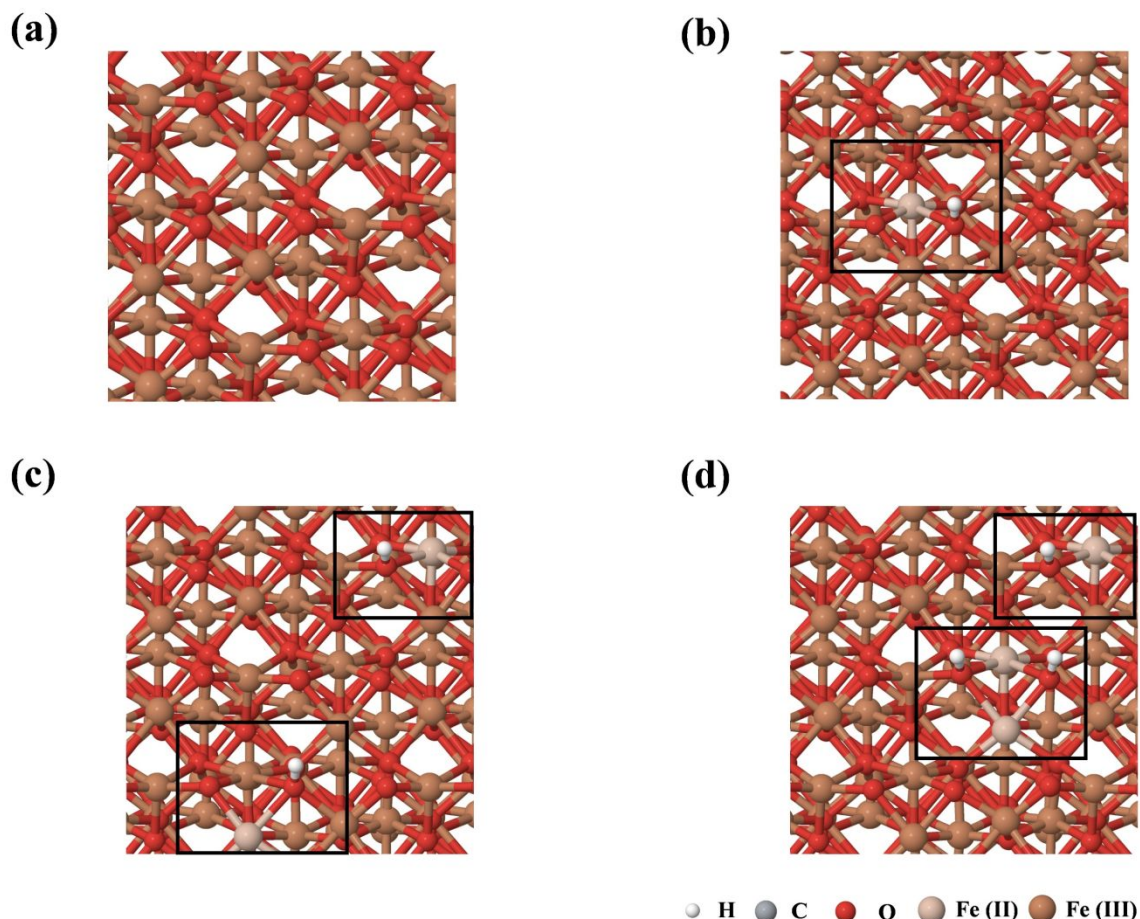


**Fig. S17** The corresponding hydrogen atoms transferring away from the reaction site in the pre-activation process calculations (Fig. 4) to avoid over-reduction. **a)** The bare H parking slab corresponding to reaction slab 1 and 2; **b)** One-H parking slab corresponding to reaction slab 3 and 4; **c)** Two-H parking slab corresponding to reaction slab 5, 6, 7, 11 and 12. The abstracted H in step 7 is parked at the nearby  $O_{2c}$  site for the occurrence of the 3<sup>rd</sup> HAT before it further transfers to the parking slab; **d)** Three-H parking slab corresponding to reaction slab 8, 9 and 10. One H atom will transfer back from the parking slab to the reaction site for water formation in the slab 11 and 12. The intention of adapting such a H parking slab in our calculation is to avoid the reaction slab from over-reduction, which can be potentially caused by the size constraints of the reaction slab included in DFT calculations, but not likely in reality given the large surface area of the catalyst. The calculated energy difference of such H transfer process is negligible and the activation barrier with transition-states calculation is sufficiently low for thermal catalysis, as illustrated in Fig. S20.



## CH<sub>4</sub> adsorption on different sites

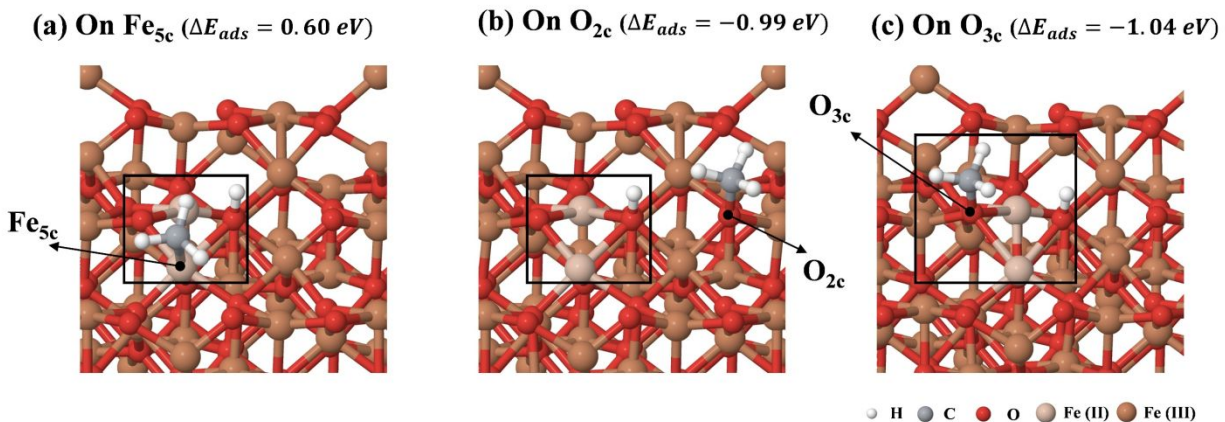


**Fig. S18** CH<sub>4</sub> adsorption with calculated energetic changes on a) an Fe<sub>5c</sub> site; b) an O<sub>2c</sub> site; c) an O<sub>3c</sub> site. The Fe reduction sites are the same in all scenarios. The reaction site is highlighted by the black box. Metal atoms are normally taken as the adsorption sites for CH<sub>4</sub>, however, this is not the case according to our calculation. We find that methane adsorption on oxygen is more favorable than that on Fe. Additionally, compared to the lower-coordinated O<sub>2c</sub>, CH<sub>4</sub> adsorbs more favorably on the O<sub>3c</sub> with a more negative energy change. This abnormal favorable adsorption is ascribed to the short O<sub>3c</sub>–O<sub>3c</sub> distance and the antiferromagnetic characteristic of the bridged diiron couple.

## Proposed electron transfer processes

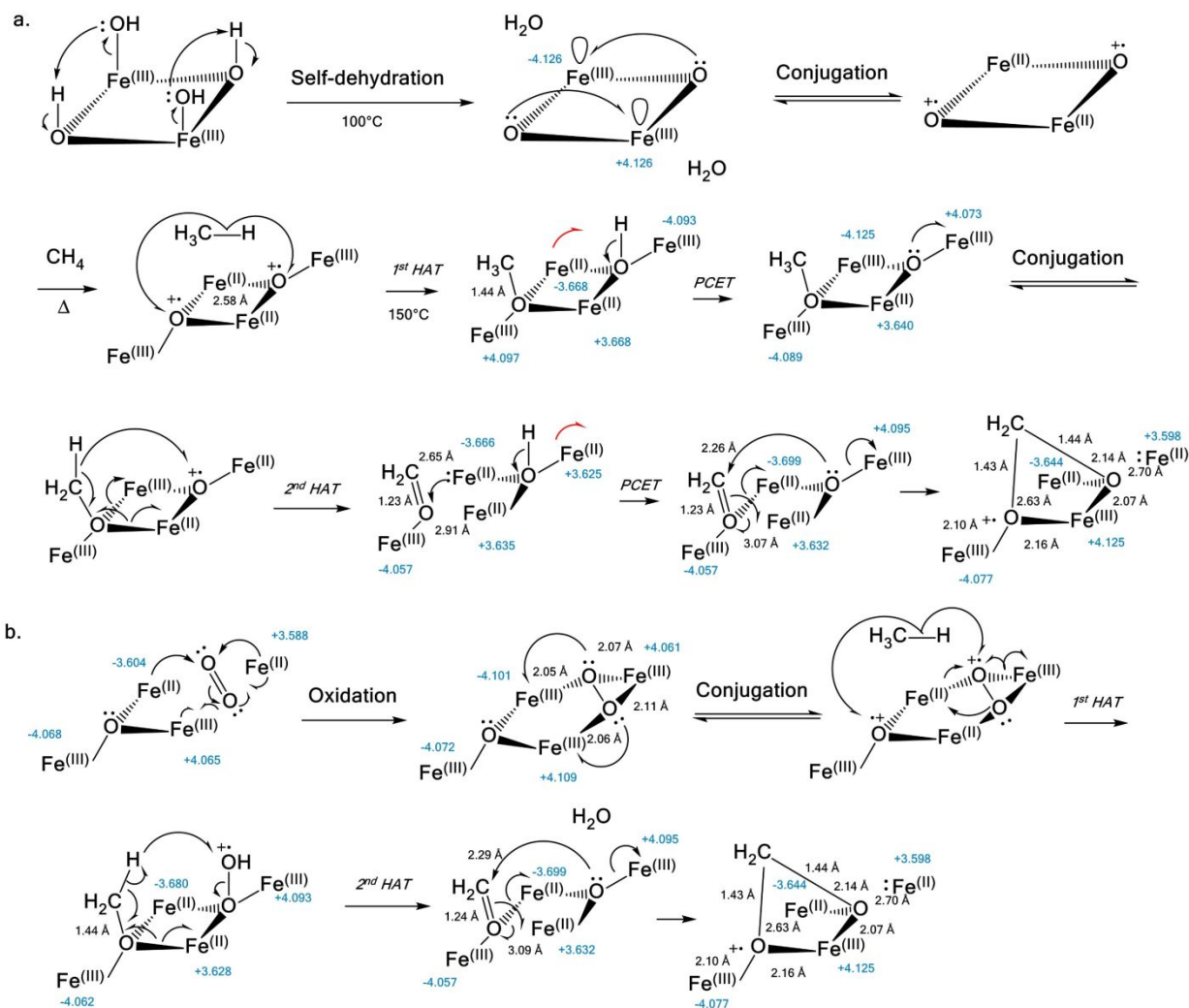


**Fig. S19** Proposed electron transfer processes during the CMC reaction on hematite. **a)** The oxygen-centered radical species can be generated by the conjugation of the lone-paired electrons on O<sub>3c</sub> with the neighboring Fe<sub>5c</sub> as a valence tautomeric transition after self-dehydration, which can activate CH<sub>4</sub> via thermal hydrogen-atom transfer (HAT) in the pre-activation process in the absence of molecular oxygen; The red arrow represents the electron transfer to the H atom parking slab in conjunction with a proton transfer via PCET process; **b)** Proposed CH<sub>4</sub> activation pathway via molecular dioxygen assistance in the catalytic cycle. The oxidation states of Fe centers were theoretically determined by computing atomic magnetic moments, which are related to the number of unpaired electrons in the *d* orbitals. For example, Fe(III) center has five unpaired 3*d* electrons while Fe(II) has four unpaired 3*d* electrons. Correspondingly the atomic magnetic moments (labelled in blue) are  $\pm 4.1$  and  $\pm 3.7$  for Fe(III) and Fe(II) centers, respectively. The deviation of computed magnetic moments from the theoretical values is due to the

definition of atomic boundary by the Wigner-Seitz radius to partition the spin density. Only inside the Wigner-Seitz radius of a specific atom the spin density is integrated to calculate the atomic magnetic moments in the algorithm. The Wigner-Seitz radius for Fe, O, C, and H is 1.302, 0.820, 0.863, and 0.370 in the unit of Å, respectively.

## Calculated energy barrier of the PCET process

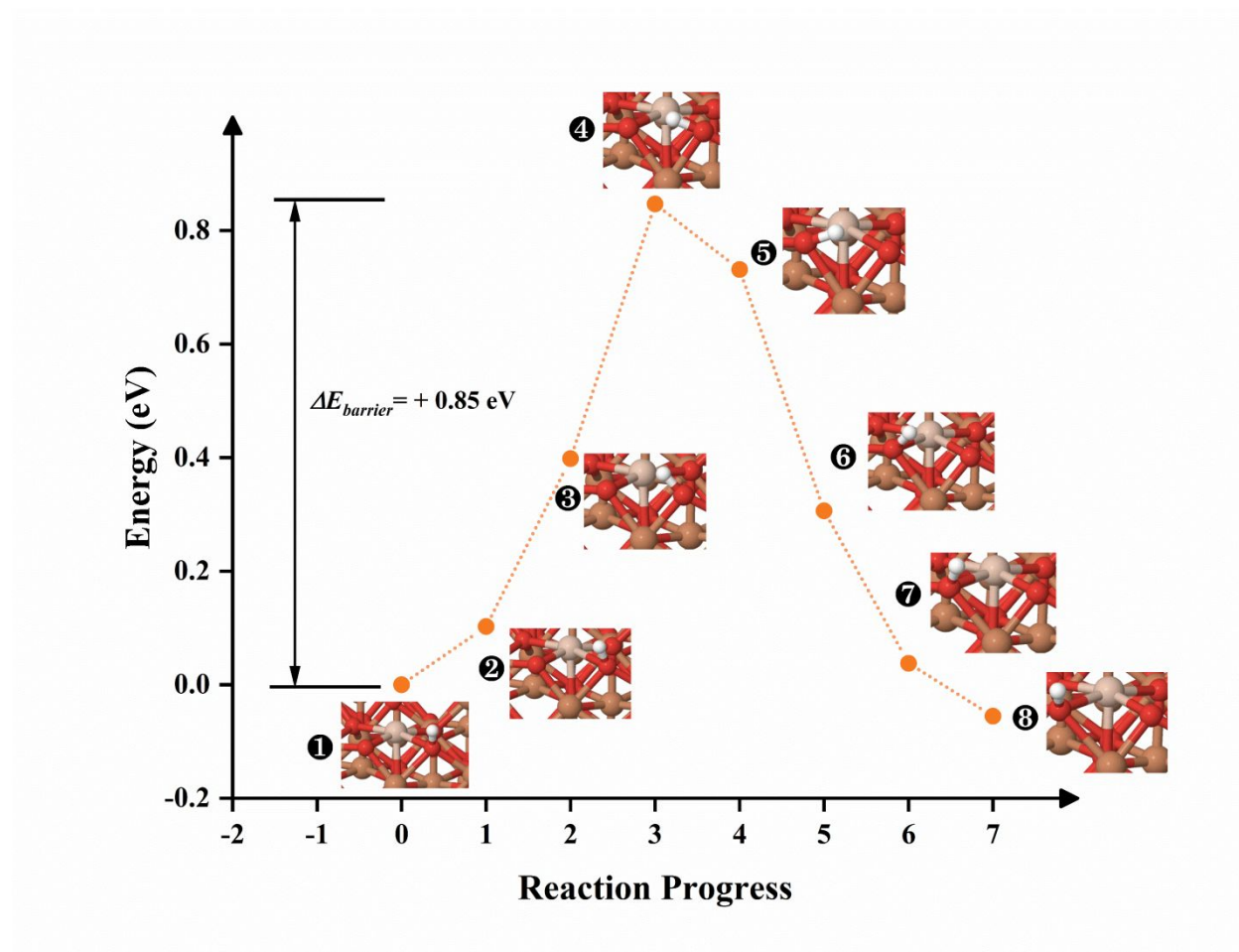


**Fig. S20** Calculated transition states of proton-coupled electron transfer (PCET) process with an energy barrier of 0.85 eV. The geometry number 1 stands for the beginning point and the number 8 is the final state. Geometry 4 is found to be the transition state with the highest potential energy on the surface. The total energy difference before and after the proton transfer is negligible (1 vs 8).



# Magnetic Moment Parameters

**Table S2.** Magnetic moment parameters for all calculations

<b>Pre-Activation Cycle Geometry</b>	
Step 1	24*5.0 24*-5.0
Step 2	18*5.0 1*4.0 5*5.0 24*-5.0
Step 3	18*5.0 1*4.0 5*5.0 19*-5.0 1*-4.0 4*-5.0
Step 4	18*5.0 1*4.0 4*5.0 1*4.0 19*-5.0 1*-4.0 4*-5.0
Step 5	N/A
Step 6	N/A
Step 7	N/A
Step 8	18*5.0 1*4.0 4*5.0 1*4.0 19*-5.0 1*-4.0 4*-5.0
Step 9 (a)	18*5.0 1*4.0 5*5.0 24*-5.0
Step 9 (b)	18*5.0 1*4.0 5*5.0 19*-5.0 1*-5.0 4*-5.0
Step 10	18*5.0 1*4.0 4*5.0 1*4.0 19*-5.0 1*-4.0 4*-5.0
Step 11	N/A
Step 12	N/A
<b>Hydrogen Parking Slab Geometry</b>	
Hematite Slab with 0 Hydrogen atom	24*5.0 24*-5.0
Hematite Slab with 1 Hydrogen atoms	18*5.0 1*4.0 5*5.0 24*-5.0
Hematite Slab with 2 Hydrogen atoms	20*5.0 1*4.0 3*5.0 22*-5.0 1*-4.0 1*-5.0
Hematite Slab with 3 Hydrogen atoms	18*5.0 1*4.0 5*5.0 19*-5.0 1*-4.0 2*-5.0 1*-4.0 1*-5.0
<b>Catalytic Cycle Geometry</b>	
Step 1	18*5.0 1*4.0 5*5.0 19*-5.0 1*-4.0 4*-5.0
Step 2	24*5.0 24*-5.0
Step 3	18*5.0 1*4.0 5*5.0 19*-5.0 1*-4.0 4*-5.0
Step 4	18*5.0 1*4.0 5*5.0 19*-5.0 1*-4.0 4*-5.0
Step 5	18*5.0 1*5.0 4*5.0 1*4.0 19*-5.0 1*-4.0 4*-5.0
Step 6	18*5.0 1*4.0 3*5.0 1*4.0 1*5.0 19*-5.0 1*-4.0 2*-5.0 1*-4.0 1*-5.0
Step 7	18*5.0 1*5.0 3*5.0 1*4.0 1*5.0 19*-5.0 1*-5.0 2*-5.0 1*-4.0 1*-5.0
Step 8	18*5.0 1*4.0 3*5.0 1*4.0 1*5.0 19*-5.0 1*-4.0 2*-5.0 1*-4.0 1*-5.0
<b>Frequency Calculation Geometry</b>	
-OCH <sub>3</sub>	18*5.0 1*4.0 5*5.0 19*-5.0 1*-4.0 4*-5.0
Bidentate formate	18*5.0 1*4.0 3*5.0 1*4.0 1*5.0 19*-5.0 1*-4.0 2*-5.0 1*-4.0 1*-5.0
Monodentate formate	20*5.0 3*4.0 1*5.0 18*-5.0 1*-4.0 2*-5.0 2*-4.0 1*-5.0
<b>Hydrogen Transition States Geometry (all geometries are same)</b>	
24*5.0 19*-5.0 1*-4.0 4*-5.0	
<b>Different CH<sub>4</sub> Dissociation Sites</b>	
CH <sub>4</sub> to Fe <sub>sc</sub>	18*5.0 1*4.0 5*5.0 19*-5.0 1*-4.0 4*-5.0
CH <sub>4</sub> to O <sub>2c</sub>	23*5.0 1*4.0 19*-5.0 1*-4.0 4*-5.0

a. All modules contain 48 iron atoms;

b. For all modules, the magnetic moment of elements other than Iron are set at 0.0.

## Reference

1. Cargnello M, Jaén JJD, Garrido JCH, Bakmutsky K, Montini T, Gámez JJC, *et al.* Exceptional Activity for Methane Combustion over Modular Pd@CeO<sub>2</sub> Subunits on Functionalized Al<sub>2</sub>O<sub>3</sub>. *Science*. **337**, 713-717 (2012).
2. Lou Y, Ma J, Hu W, Dai Q, Wang L, Zhan W, *et al.* Low-Temperature Methane Combustion over Pd/H-ZSM-5: Active Pd Sites with Specific Electronic Properties Modulated by Acidic Sites of H-ZSM-5. *ACS Catal.* **6**, 8127-8139 (2016).
3. Venezia AM, Di Carlo G, Pantaleo G, Liotta LF, Melaet G, Kruse N. Oxidation of CH<sub>4</sub> over Pd supported on TiO<sub>2</sub>-doped SiO<sub>2</sub>: Effect of Ti(IV) loading and influence of SO<sub>2</sub>. *Appl. Catal., B*. **88**, 430-437 (2009).
4. Persson K, Ersson A, Jansson K, Iverlund N, Järås S. Influence of co-metals on bimetallic palladium catalysts for methane combustion. *J. Catal.* **231**, 139-150 (2005).
5. Wang Y, Arandiyán H, Scott J, Akia M, Dai H, Deng J, *et al.* High Performance Au–Pd Supported on 3D Hybrid Strontium-Substituted Lanthanum Manganite Perovskite Catalyst for Methane Combustion. *ACS Catal.* **6**, 6935-6947 (2016).
6. Águila G, Gracia F, Cortés J, Araya P. Effect of copper species and the presence of reaction products on the activity of methane oxidation on supported CuO catalysts. *Appl. Catal., B*. **77**, 325-338 (2008).
7. Yu Q, Wang C, Li X, Li Z, Wang L, Zhang Q, *et al.* Engineering an effective MnO<sub>2</sub> catalyst from LaMnO<sub>3</sub> for catalytic methane combustion. *Fuel*. **239**, 1240-1245 (2019).
8. Zhang L, Zhang Y, Dai H, Deng J, Wei L, He H. Hydrothermal synthesis and catalytic performance of single-crystalline La<sub>2-x</sub>Sr<sub>x</sub>CuO<sub>4</sub> for methane oxidation. *Catal. Today*. **153**, 143-149 (2010).
9. Tao FF, Shan J-j, Nguyen L, Wang Z, Zhang S, Zhang L, *et al.* Understanding complete oxidation of methane on spinel oxides at a molecular level. *Nature Communications*. **6**, 7798 (2015).
10. Wang H, Chen C, Zhang Y, Peng L, Ma S, Yang T, *et al.* In situ oxidation of carbon-encapsulated cobalt nanocapsules creates highly active cobalt oxide catalysts for hydrocarbon combustion. *Nature Communications*. **6**, 7181 (2015).
11. Zhao S, Li J. Silver–Cobalt Oxides Derived from Silver Nanoparticles Deposited on Layered Double Hydroxides for Methane Combustion. *ChemCatChem*. **7**, 1966-1974 (2015).
12. Snyder BE, Bols ML, Schoonheydt RA, Sels BF, Solomon EI. Iron and copper active sites in zeolites and their correlation to metalloenzymes. *Chem. Rev.* **118**, 2718-2768 (2017).